Supplementary material for "*Evidence that superstructures comprise of self-similar coherent motions in high Re_τ boundary layers*"

Rahul Deshpande[1]†, Charitha M. de Silva[2], and Ivan Marusic[1]

[1]Department of Mechanical Engineering, University of Melbourne, Parkville, VIC 3010, Australia

[2]School of Mechanical and Manufacturing Engineering, University of New South Wales, Sydney, NSW 2052, Australia

1. Detailed methodology to identify and extract superstructures

Figure 1 describes the step-by-step procedure of applying the three thresholds (discussed in the manuscript) to identify, extract and characterize flow fields associated with (SS) and not associated ($noSS$) with turbulent superstructures:

Step 1: We begin with an instantaneous flow field of the streamwise velocity fluctuations (u). For this procedure, we have considered the same flow field as plotted in figure 3(a) of the main manuscript.

Step 2: First, the threshold associated with the streamwise turbulent kinetic energy is applied on the PIV flow field (criteria (i) in the manuscript). This enforces any values of $|u(x,z)| \leq \sqrt{\overline{u^2(z)}}$ to zero in the PIV flow field.

One can note from the figure that imposing this threshold essentially removes all weak features (predominantly small-scale), but preserves the intermediate- and large-scaled (prominent) motions, which are the focus of the present study.

Step 3: Next, coherent regions of u-momentum are identified across the PIV flow field. This is facilitated by the *regionprops* function in MATLAB, which defines bounding (rectangular) boxes around each individual structure, estimates the area it covers, etc. As an example, step 3 in the figure shows the bounding boxes (in dashed black lines) around four such u-motions (out of $\sim$70) identified by the *regionprops* function for the given PIV u-flow field.

Step 4: Once the bounding boxes are defined for each identified u-motion, they are filtered to select only those structure(s) which have streamwise (L_x) and wall-normal extents (Δz) of their bounding boxes greater than the thresholds set for identifying a superstructure. In the present study, we use threshold for the streamwise extent, $L_x > 3\delta$. While, the lower bound of the bounding box should lie below $z^+ \lesssim 2.6\sqrt{Re_\tau}$ and the upper bound should extend at least up to the middle of the boundary layer, $z^+ \gtrsim 0.5Re_\tau$. For the PIV datasets analyzed in the present study, we found at most *one* u-structure in each PIV flow field which satisfied the three thresholds.

Step 4 in figure 1 shows a $-u$ superstructure conforming to the three thresholds, which has been indicated by a dashed green box. Length and height of this bounding box (i.e. superstructure) has been indicated by L_x^{SS} and Δz^{SS} simply for local reference. Nearly

† Email address for correspondence: raadeshpande@gmail.com

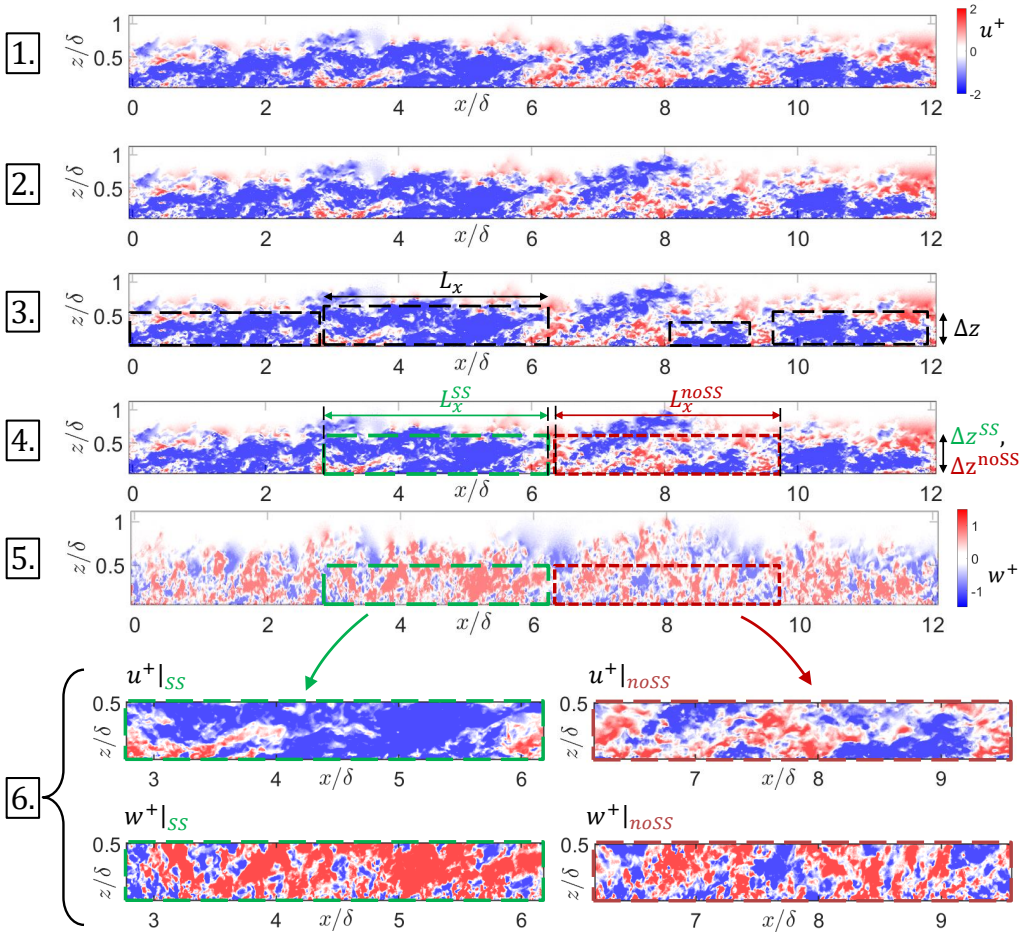

FIGURE 1. Flow chart based description of the identification, extraction and characterization of SS and $noSS$ regions analyzed in the manuscript. (1-5) Instantaneous (1-4) u^+ and (5) w^+-fluctuations from the LFOV PIV dataset at $Re_\tau \approx 2500$. The dashed green box in (4,5) identifies a low-momentum turbulent superstructure ($-u_{ss}$) of length L_x based on the turbulent superstructure algorithm described in the text. (6) shows an expanded view of the u- and w-fluctuations within $-u_{ss}$, as identified in (4,5), respectively. Alternatively, the dashed brown box in (4,5) represents flow field of the same length×height as the dashed green box, but not associated with a turbulent superstructure ($noSS$). (6) shows an expanded view of the u- and w-fluctuations within $noSS$ identified in (4,5), respectively.

77% of the surface area within this box corresponds to this $-u$ superstructure (for this particular example), suggesting that choosing a rectangular box doesn't significantly add non-superstructure related flow features. Once a superstructure has been identified in a PIV image, the algorithm next identifies another region of the same length×height in the same PIV flow field, which can be associated with $noSS$ (i.e. $L_x^{noSS} = L_x^{SS}$ and $\Delta z^{noSS} = \Delta z^{SS}$). The region corresponding to $noSS$ is fixed in the same wall-normal range as the SS but is in a different streamwise location to avoid overlapping with a superstructure. Step 4 in figure 1 shows a region identified by the algorithm as $noSS$, which is indicated by a dashed brown box. It is evident that the flow field within the $noSS$ has no very-large-scale u-motions.

Step 5: With the 2-D u-flow field associated with SS and $noSS$ identified in step 4, next step is to identify the corresponding regions in the w-flow field (of same length×height in the same pixel locations as in u-field). They have been indicated for the corresponding w-flow field in step 5 of the figure 1.

Step 6: The next and final step is to extract and save the 2-D u- and w-flow fields within the bounding boxes associated with the SS and $noSS$ regions, identified in step 4 and 5. This is shown in step 6 of figure 1.

The procedure described above is for a particular PIV u-flow field at $Re_\tau \approx 2500$ within which a superstructure was identified. The procedure from steps 1-4 is repeated on all 3000 PIV images acquired at each Re_τ. Steps 5-6 are implemented only for u-flow fields within which a superstructure is identified. On an average, we found 300 u-structures (across 3000 PIV images at each Re_τ) that could be classified as superstructures (based on the selected thresholds). On an average, 80% of the surface area of the bounding boxes, extracted from the PIV u-flow fields, is filled by the u-superstructures. Hence, the conditional statistics estimated based on the extracted 2-D flow fields can be associated with u-superstructures with reasonable confidence.

2. Support from synthetically generated fields

The scaling arguments presented in the main manuscript lend empirical support in favour of geometrically self-similar attached eddies, concatenating along the streamwise direction, form the superstructures. Here, we make use of synthetically generated flow fields to show that the statistical analysis presented in the main manuscript is consistent with the present hypothesis. This is exhibited by investigating the scalings/trends of spectra and correlations computed from the synthetic fields. Three different types of synthetic fields are chosen to present convincing support for the present hypothesis, each of which comprises of a 'hairpin' or simple arch-shaped (Λ) eddy as the representative coherent structure/'hierarchy' to model the inertial region of a boundary layer (Head & Bandyopadhyay 1981; Adrian *et al.* 2000; Wu & Moin 2009; Dennis & Nickels 2011). The three fields essentially represent characteristically different distributions of variable sized Λ-eddies in the flow field, in a way that would test the hypothesis brought out by the empirical analysis presented in the main manuscript. For this, the simplest version of the Λ-eddy is considered, which is made up of two vortex rods arranged in a Λ-shape, with each rod comprising of a Gaussian distribution of vorticity about its core. Based on the previous experimental evidence (Head & Bandyopadhyay 1981; Deshpande *et al.* 2019), each of these Λ-eddies are forced to be inclined forwards, at 45° with respect to the mean flow direction. The three component velocity fields associated with each eddy is obtained by performing Biot-Savart calculations. Each Λ-eddy also has a corresponding image eddy in the plane of the wall, which is implemented to enforce impermeability conditions at the wall ($w = 0$ at $z = 0$). Figure 2 of this document schematically depicts the three synthetic fields considered here, with the green rods representing the vorticity carrying Λ-eddies and the red and blue iso-contours representing the induced $+w$ and -w, respectively.

In case of the synthetic field 1, the inertial region of the boundary layer is simply represented by superposition of six hierarchies of the Λ-eddies, of varying sizes ($\mathcal{H}_i$; with i being the hierarchy number) and population densities, randomly distributed in the flow field. Figure 2(a) shows a schematic of four Λ-eddy hierarchies (in green), organized randomly in the flow domain, for representative purposes. For convenience in setting up this synthetic field, the height ($\mathcal{H}$) of the relatively taller hierarchy is defined to be twice the size of the previous hierarchy (i.e. $\mathcal{H}_{i+1} \sim 2\mathcal{H}_i$), while the population

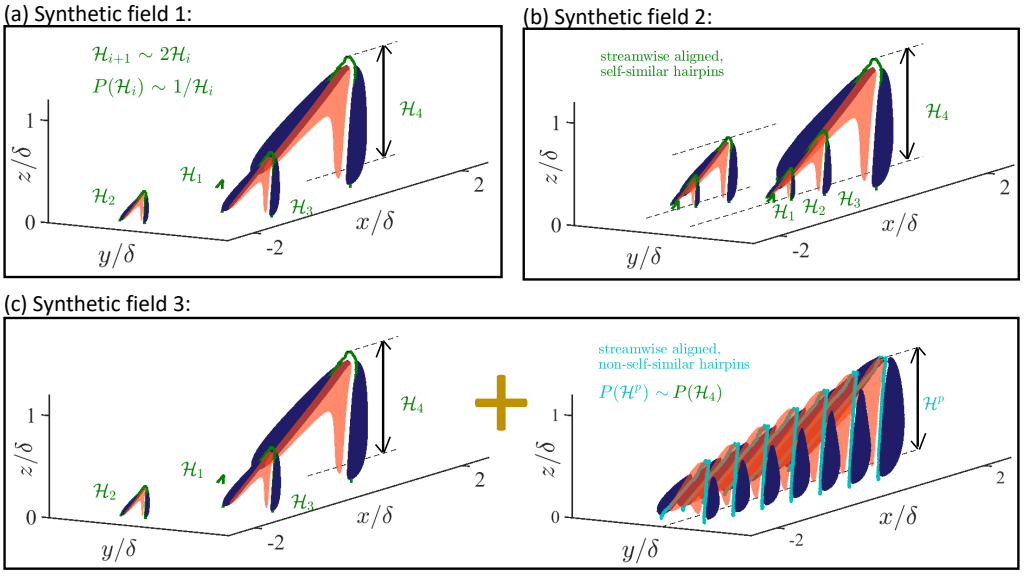

FIGURE 2. Schematic describing the various 3-D synthetic flow fields generated by hierarchies ($\mathcal{H}_i$, $i = 1,2,....$) of Λ-shaped vortex rods (in green) distributed in the flow domain. Blue and red regions represent the 3-D iso-contours of -w and +w induced due to the vorticity in the individual hairpins. Both, (a) synthetic field 1 and (b) synthetic field 2 comprise of geometrically self-similar Λ-eddies, with the only difference being these eddies are distributed randomly in space in field 1, while the various hierarchies are forced to align along x in field 2 to form a streamwise elongated motion (as seen in figure 2(c,e) of the main manuscript). (c) Synthetic field 3 is essentially a combination of synthetic field 1 in (a) and multiple geometrically non-self-similar Λ-eddies aligned along x to also form an elongated motion. $P(\mathcal{H}_i)$ represents the population density of the hierarchy, $\mathcal{H}_i$.

density varies inversely proportional to the size of the hierarchy ($\mathcal{P}(\mathcal{H}_i) \sim 1/\mathcal{H}_i$). The height of the largest hierarchy is, by definition, the boundary layer thickness δ. Similar conventions have been followed in previous studies (de Silva *et al.* 2016; Deshpande *et al.* 2021) to set up attached eddy model simulations, which ensure a geometrically self-similar variation in size of the Λ-eddy hierarchies introduced in the present synthetic flow fields. A noteworthy difference between the present and past simulations, however, is the consideration of an individual Λ-eddy as the representative eddy for the present synthetic fields, as opposed to that of a Λ-eddy packet in the previous simulations (which is the recommended pathway). It is owing to this reason that the present fields can't be expected to replicate the same statistical trends/features as those noted in the previous simulations. The choice for the present study, however, is justified considering the aim of investigating whether the spatial organization of smaller self-similar motions can lead to streamwise elongated motions.

Synthetic field 2 comprises essentially the same Λ-eddy hierarchies (with the same population density) as in synthetic field 1, with the only difference being that the hierarchies are forced to be streamwise aligned in case of the former, as per the concatenation hypothesis (Adrian *et al.* 2000). The synthetic field 2, hence, is a conceptual representation of the experimental observations presented in the main manuscript, that suggests superstructures may likely be concatenations of geometrically self-similar motions. Figure 2(b) schematically represents the unique spatial distribution of the various hierarchies of Λ-eddies in the case of synthetic field 2, with hierarchies $\mathcal{H}_4$, $\mathcal{H}_3$ and $\mathcal{H}_2$ only organized in certain streamwise alignments to maintain the same population density

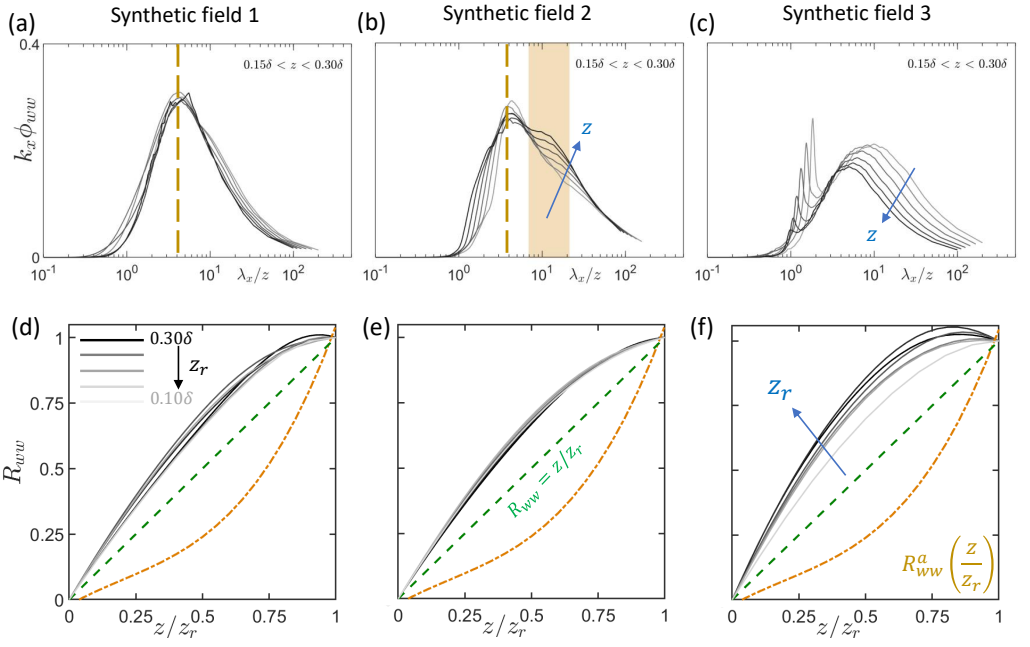

FIGURE 3. (a-c) Premultiplied 1-D spectra of w-fluctuations plotted vs λ_x/z at various wall-normal locations of the synthetic flow fields. (d-f) Cross-correlation of w-fluctuations measured at z and z_r, normalized by $\overline{w^2}(z_r)$ at various z_r. In (a-b), the dashed golden line represents the linear scaling, $\lambda_x \sim z$. In (d-f), the dashed green line corresponds to the linear relationship, z/z_r while dash-dotted golden line corresponds to R^a_{ww} defined in (3.2) of the main manuscript. Shaded yellow background in (b) relates to the increase in large-scale energy.

as in synthetic field 1. Consequently, while synthetic field 2 would be expected to reveal recurrent streamwise elongated motions (superstructures) in the instantaneous flow field, synthetic field 1 won't. In contrast to these two fields, synthetic field 3 is a conceptual representation of a hypothetical scenario wherein a superstructure has no association with the geometrically self-similar (i.e. z-scaled) inertia-dominated motions. For this purpose, synthetic field 3 considers multiple streamwise aligned non-self-similar Λ-eddies which are added to the same flow field as the synthetic field 1. Thus, comparing and contrasting the scalings/trends exhibited by the velocity statistics, from these three synthetic fields, could shed light on whether the streamwise alignment of self-similar motions explains the statistical observations in the main manuscript.

Figure 3 of this document depicts the premultiplied 1-D spectra of the w-fluctuations (figures 3(a-c)) and the two-point correlations (R_{ww}; figure 3(d-f)) from the three synthetic fields considered in the present study. Both $k_x\phi_{ww}$ and R_{ww} from synthetic field 1 exhibit z-scalings consistent with that expected from a flow field made up of purely self-similar attached eddies. The trend of the statistics are qualitatively similar to that observed for the real flow in figures 5(a) and 6(a-d) of the main manuscript; there is, however, a quantitative mismatch in the linear scaling for $k_x\phi_{ww}$ and least-squares fit obtained for R_{ww}. Quantitative estimates depend on the exact shape and vorticity defined for the representative Λ-eddy, which hasn't been explored in the present study, to maintain simplicity.

Considering synthetic field 2, the same z-scaling (as noted for field 1) is also clearly noted for both $k_x\phi_{ww}$ and R_{ww}. One can also note an interesting trend of enhanced energy

at large λ_x (highlighted with shaded background), which can be associated with the imposed streamwise alignment of the Λ-eddy hierarchies. The good correspondence of the empirical observations with synthetic field 2 confirms the observations can be associated with large-scale spatial organization of the geometrically self-similar eddies within the superstructures. Interestingly, when the spectra and correlations are investigated for synthetic field 3, neither of them exhibit z-scalings. Both $k_x\phi_{ww}$ and R_{ww} clearly depict a trend dependent on z_r for this field, which is not noted in synthetic fields 1 and 2, or in the experimental statistics. This deviation from the z-scaling can be associated with the consideration of streamwise aligned non-self-similar eddies in synthetic field 3, further reaffirming the relationship between the attached eddies and superstructures.

REFERENCES

Adrian, R. J., Meinhart, C. D. & Tomkins, C. D. 2000 Vortex organization in the outer region of the turbulent boundary layer. *Journal of Fluid Mechanics* **422**, 1–54.

Dennis, D.J.C. & Nickels, T.B. 2011 Experimental measurement of large-scale three-dimensional structures in a turbulent boundary layer. Part 1. Vortex packets. *Journal of Fluid Mechanics* **673**, 180–217.

Deshpande, R., Monty, J.P. & Marusic, I. 2019 Streamwise inclination angle of large wall-attached structures in turbulent boundary layers. *Journal of Fluid Mechanics* **877**, R4.

Deshpande, R., de Silva, C. M., Lee, M., Monty, J. P. & Marusic, I. 2021 Data-driven enhancement of coherent structure-based models for predicting instantaneous wall turbulence. *International Journal of Heat and Fluid Flow* **92**, 108879.

Head, M. R. & Bandyopadhyay, P. 1981 New aspects of turbulent boundary-layer structure. *Journal of Fluid Mechanics* **107**, 297–338.

de Silva, C. M., Hutchins, N. & Marusic, I. 2016 Uniform momentum zones in turbulent boundary layers. *Journal of Fluid Mechanics* **786**, 309–331.

Wu, X. & Moin, P. 2009 Direct numerical simulation of turbulence in a nominally zero-pressure-gradient flat-plate boundary layer. *Journal of Fluid Mechanics* **630**, 5–41.